THERMAL PROPERTIES AND GROUND-STATE STRUCTURES OF PURE AND ALLOY NANOCLUSTERS VIA MOLECULAR DYNAMICS SIMULATION

ONG YEE PIN

UNIVERSITI SAINS MALAYSIA

2018

THERMAL PROPERTIES AND GROUND-STATE STRUCTURES OF PURE AND ALLOY NANOCLUSTERS VIA MOLECULAR DYNAMICS SIMULATION

by

ONG YEE PIN

Thesis submitted in fulfillment of the requirements
for the degree of
Master of Science

March 2018

ACKNOWLEDGEMENT

I would like to thank my supervisor, Dr Yoon Tiem Leong for his patience and guidance throughout my study. Besides, I would like to show my gratitude towards Dr Lim Thong Leng for his kind advice, generous help and respect for the originality of my work.

I would like to acknowledge Prof. Lai San Kiong and Dr. Yen Tsung Wen from National Central University, Taiwan for generously providing guidance and computational tools used in this thesis.

I am grateful to my labmates (Yee Yeen, Wei Chun, Tjun Kit, Thong Yan, Pin Wai, Timothy and Robin) for providing an encouraging, joyful and lively surrounding. Last but not least, I would like to acknowledge my family members and friends for their wholehearted support.

TABLE OF CONTENTS

Acknowledgements		ii
Table of Contents		iii
List of Tables		vii
List of Figures		viii
List of Abbreviations		xiv
List of Symbols		xv
Abstrak		xviii
Abstract		xx
CHAPTER 1 – INTRODUCTION		**1**
1.1	Nanoclusters	1
1.2	Importance of Nanoclusters	2
1.3	Gold-Platinum Nanoclusters	4
1.4	Objective of Study	5

CHAPTER 2 – THEORETICAL BACKGROUND AND METHODOLOGIES **7**

2.1 Parallel Tempering Multicanonical Basin Hopping Plus Genetic Algorithm (PTMBHGA) 8

2.1.1 Gupta Many Body Potential 9

2.1.2 Genetic Algorithm 10

2.1.3 Basin Hopping 13

2.1.4 Multicanonical Basin Hopping 16

2.1.5 PTMBHGA Working Parameters 16

2.2 Thermal Properties of Nanoclusters 18

2.2.1 Brownian Type Isothermal Molecular Dynamics Simulations 19

2.2.2 Procedures of Molecular Dynamics Simulations 21

2.3 Ultrafast Shape Recognition 22

CHAPTER 3 – RESULTS AND DISCUSSION **27**

3.1 Ground-State Structure for Nanoclusters 27

3.1.1 Ground-State Structures of Pure Gold Nanoclusters 28

3.1.2 Ground-State Structures of Pure Platinum Nanoclusters 34

3.1.3 Ground-State Structures of Gold-Platinum Nanoclusters 37

CHAPTER 4 – MELTING BEHAVIOUR OF NANOCLUSTERS 41

4.1 Specific Heat 41

4.2 Lindemann Index 42

4.3 Test Case: $Au_{12}Cu_1$ 43

4.4 $Au_{32}Pt_6$ 46

4.5 Post-Processing with Ultrafast Shape Recognition 47

4.5.1 Probability Distribution Function (PDF) of Similarity Index $P(\zeta)$ 53

4.5.1.(a) 100 K 56

4.5.1.(b) 400 K 57

4.5.1.(c) 700 K 59

4.5.1.(d) 800 K 60

4.5.1.(e) Numerical Results in the 700 K - 800 K Region with Refined Temperature Resolution 62

4.5.1.(f) 900 K 65

4.5.1.(g) 1000 K 68

4.5.1.(h) 2000 K 70

4.6 Comparison between Melting Post-Processing Techniques 71

4.7 Further Verification for Ultrafast Shape Recognition 72

4.7.1 Ground-State Structure for Au_{38} 73

4.7.2 Melting Process 73

4.7.3 Ultrafast Shape Recognition for Au_{38} 74

CHAPTER 5 – CONCLUSIONS AND FUTURE STUDIES 78

5.1 Conclusion 78

5.2 Future Studies 81

Publication Lists 82

References 83

Appendix

LIST OF TABLES

		Page
Table 2.1	Gupta parameters for gold, platinum and gold platinum atoms.	10
Table 3.1	The minimum potential energy for gold nanoclusters obtained from PTMBHGA.	30
Table 3.2	Structures of gold nanoclusters with high symmetry and relative stability.	32
Table 3.3	The minimum potential energy for platinum nanoclusters obtained from PTMBHGA.	34
Table 3.4	Structures of high symmetry and relative stability platinum nanoclusters.	36
Table 3.5	The minimum potential energy for gold-platinum nanoclusters obtained from PTMBHGA.	38
Table 3.6	Structures of gold-platinum nanoclusters with high symmetry and relative stability. The army green spheres in the core of these clusters represent platinum atoms while that in the shell gold atoms.	40

LIST OF FIGURES

		Page
Figure 2.1	Flow chart of calculation procedure.	8
Figure 2.2	Flow chart of genetic algorithm in PTMBHGA.	12
Figure 2.3	Flow chart of basin hopping in PTMBHGA.	15
Figure 2.4	Flow chart of PTMBHGA.	18
Figure 2.5	The location of COM in $Au_{32}Pt_6$ ground-state structure. (Olive green represents platinum atoms and pink represents gold atoms)	24
Figure 2.6	The location of CCM atom in $Au_{32}Pt_6$ ground-state structure.	25
Figure 2.7	The location of FCM atom in $Au_{32}Pt_6$ ground-state structure.	25
Figure 2.8	The location of FCM atom in $Au_{32}Pt_6$ ground-state structure.	26
Figure 3.1	The comparison between the structures of gold nanoclusters obtained from PTMBHGA (upper) and reference (below) from Xia Wu *et al.* 2012.	29
Figure 3.2	The second energy difference plot for gold nanoclusters from size 3-55 atoms.	31
Figure 3.3	The second energy difference plot for platinum nanoclusters from size 3-55 atoms.	35
Figure 3.4	The second energy difference plot for gold-platinum nanoclusters of 38 atoms for every composition. n refers to the number of gold atom in the bimetallic clusters Au_nPt_{38-n}.	39
Figure 4.1	Graph of specific heat C_v (continuous line) and Lindemann Index δ (dotted line) against temperature for $Au_{12}Cu_1$ nanocluster.	44

Figure 4.2	Graphs of (a) specific heat C_v and (b) Lindemann Index δ against temperature for $Au_{12}Cu_1$ obtained by Yen *et al.*, 2009.	45
Figure 4.3	Graph of specific heat C_v (continuous line) and Lindemann Index δ (dotted line) against temperature for $Au_{32}Pt_6$ nanocluster.	46
Figure 4.4	USR comparison plots of atomic distance from COM at three different temperatures (a) 100 K (b) 770 K (c) 1800 K. Blue line represents a atomic distance profile of the structure at 0 K, while the black line is for atomic distances defined with respect to the temperature-dependent COM for current structure.	49
Figure 4.5	Structures of $Au_{32}Pt_6$ nanocluster with increasing temperature (a) 100 K (b) 770 K (c) 1800 K.	51
Figure 4.6	Graph of $P(\zeta)$ against ζ for $Au_{32}Pt_6$ nanocluster at $100\ \text{K} \leq T \leq 2000\ \text{K}$.	55
Figure 4.7	Graph of $P(\zeta)$ against ζ for $Au_{32}Pt_6$ nanocluster at T = 100 K.	56
Figure 4.8	(a) Atomic distance comparison graphs obtained from USR and (b), (c) structure of $Au_{32}Pt_6$ nanocluster at T = 100 K.	57
Figure 4.9	Graph of $P(\zeta)$ against ζ for $Au_{32}Pt_6$ nanocluster at T = 100 K and 400 K.	58
Figure 4.10	(a) Atomic distance comparison graphs obtained from USR and (b), (c) structure of $Au_{32}Pt_6$ nanocluster at T = 400 K.	58
Figure 4.11	Graph of $P(\zeta)$ against ζ for $Au_{32}Pt_6$ nanocluster at T = 400 K and 700 K.	59
Figure 4.12	(a) Atomic distance comparison graphs obtained from USR and (b), (c) structure of $Au_{32}Pt_6$ nanocluster at T = 700 K.	60
Figure 4.13	Graph of $P(\zeta)$ against ζ for $Au_{32}Pt_6$ nanocluster at T = 700 K and 800 K.	61
Figure 4.14	(a) Atomic distance comparison graphs obtained from USR and (b), (c) structure of $Au_{32}Pt_6$ nanocluster at T = 800 K.	62

Figure 4.15	Graph of $P(\zeta)$ against ζ for $Au_{32}Pt_6$ nanocluster at T between 700 K and 800 K.	63
Figure 4.16	Graph of $P(\zeta)$ against ζ for $Au_{32}Pt_6$ nanocluster at T = 760 K and 770 K.	64
Figure 4.17	(a) Atomic distance comparison graphs obtained from USR and (b), (c) structure of $Au_{32}Pt_6$ nanocluster at T = 760 K.	64
Figure 4.18	(a) Atomic distance comparison graphs obtained from USR and (b), (c) structure of $Au_{32}Pt_6$ nanocluster at T = 770 K.	65
Figure 4.19	Graph of $P(\zeta)$ against ζ for $Au_{32}Pt_6$ nanocluster at T = 800 K and 900 K.	67
Figure 4.20	(a) Atomic distance comparison graphs obtained from USR and (b), (c) structure of $Au_{32}Pt_6$ nanocluster at T = 900 K.	67
Figure 4.21	Graph of P(ζ) against ζ for $Au_{32}Pt_6$ nanocluster at T = 900 K and 1000 K.	69
Figure 4.22	(a) Atomic distance comparison graphs obtained from USR and (b), (c) structure of $Au_{32}Pt_6$ nanocluster at T = 1000 K.	69
Figure 4.23	Graph of $P(\zeta)$ against ζ for $Au_{32}Pt_6$ nanocluster at T = 1000 K and 2000 K.	70
Figure 4.24	(a) Atomic distance comparison graphs obtained from USR and (b), (c) structure of $Au_{32}Pt_6$ nanocluster at T = 2000 K.	70
Figure 4.25	Ground-state structure for 38 atoms gold nanocluster.	73
Figure 4.26	Specific heat C_v and Lindemann index plot for Au_{38}. The dotted line is for Lindemann index.	74
Figure 4.27	Graph of $P(\zeta)$ against ζ for Au_{38} nanocluster at $100\ \text{K} \leq T \leq 2000$ K.	76
Figure 4.28	Graph of $P(\zeta)$ against ζ for Au_{38} nanocluster at T = 500 K and 550 K.	77
Figure 4.29	Structure for 38 gold nanocluster at T = 550 K.	77

Figure A 1	Atomic distance comparison graphs obtained from USR and structure of $Au_{32}Pt_6$ nanocluster at T = 100 K. (Olive green represents platinum atoms and pink represents gold atoms)	87
Figure A 2	Atomic distance comparison graphs obtained from USR and structure of $Au_{32}Pt_6$ nanocluster at T = 200 K.	88
Figure A 3	Atomic distance comparison graphs obtained from USR and structure of $Au_{32}Pt_6$ nanocluster at T = 300 K.	89
Figure A 4	Atomic distance comparison graphs obtained from USR and structure of $Au_{32}Pt_6$ nanocluster at T = 400 K.	90
Figure A 5	Atomic distance comparison graphs obtained from USR and structure of $Au_{32}Pt_6$ nanocluster at T = 500 K.	91
Figure A 6	Atomic distance comparison graphs obtained from USR and structure of $Au_{32}Pt_6$ nanocluster at T = 600 K.	92
Figure A 7	Atomic distance comparison graphs obtained from USR and structure of $Au_{32}Pt_6$ nanocluster at T = 650 K.	93
Figure A 8	Atomic distance comparison graphs obtained from USR and structure of $Au_{32}Pt_6$ nanocluster at T = 700 K.	94
Figure A 9	Atomic distance comparison graphs obtained from USR and structure of $Au_{32}Pt_6$ nanocluster at T = 710 K.	95
Figure A 10	Atomic distance comparison graphs obtained from USR and structure of $Au_{32}Pt_6$ nanocluster at T = 720 K.	96
Figure A 11	Atomic distance comparison graphs obtained from USR and structure of $Au_{32}Pt_6$ nanocluster at T = 730 K.	97
Figure A 12	Atomic distance comparison graphs obtained from USR and structure of $Au_{32}Pt_6$ nanocluster at T = 740 K.	98
Figure A 13	Atomic distance comparison graphs obtained from USR and structure of $Au_{32}Pt_6$ nanocluster at T = 750 K.	99
Figure A 14	Atomic distance comparison graphs obtained from USR and structure of $Au_{32}Pt_6$ nanocluster at T = 760 K.	100
Figure A 15	Atomic distance comparison graphs obtained from USR and structure of $Au_{32}Pt_6$ nanocluster at T = 770 K.	101

Figure A 16 Atomic distance comparison graphs obtained from USR and structure of $Au_{32}Pt_6$ nanocluster at T = 780 K. 102

Figure A 17 Atomic distance comparison graphs obtained from USR and structure of $Au_{32}Pt_6$ nanocluster at T = 790 K. 103

Figure A 18 Atomic distance comparison graphs obtained from USR and structure of $Au_{32}Pt_6$ nanocluster at T = 800 K. 104

Figure A 19 Atomic distance comparison graphs obtained from USR and structure of $Au_{32}Pt_6$ nanocluster at T = 850 K. 105

Figure A 20 Atomic distance comparison graphs obtained from USR and structure of $Au_{32}Pt_6$ nanocluster at T = 900 K. 106

Figure A 21 Atomic distance comparison graphs obtained from USR and structure of $Au_{32}Pt_6$ nanocluster at T = 950 K. 107

Figure A 22 Atomic distance comparison graphs obtained from USR and structure of $Au_{32}Pt_6$ nanocluster at T = 1000 K. 108

Figure A 23 Atomic distance comparison graphs obtained from USR and structure of $Au_{32}Pt_6$ nanocluster at T = 1010 K. 109

Figure A 24 Atomic distance comparison graphs obtained from USR and structure of $Au_{32}Pt_6$ nanocluster at T = 1020 K. 110

Figure A 25 Atomic distance comparison graphs obtained from USR and structure of $Au_{32}Pt_6$ nanocluster at T = 1030 K. 111

Figure A 26 Atomic distance comparison graphs obtained from USR and structure of $Au_{32}Pt_6$ nanocluster at T = 1040 K. 112

Figure A 27 Atomic distance comparison graphs obtained from USR and structure of $Au_{32}Pt_6$ nanocluster at T = 1050 K. 113

Figure A 28 Atomic distance comparison graphs obtained from USR and structure of $Au_{32}Pt_6$ nanocluster at T = 1100 K. 114

Figure A 29 Atomic distance comparison graphs obtained from USR and structure of $Au_{32}Pt_6$ nanocluster at T = 1200 K. 115

Figure A 30 Atomic distance comparison graphs obtained from USR and structure of $Au_{32}Pt_6$ nanocluster at T = 1300 K. 116

Figure A 31 Atomic distance comparison graphs obtained from USR and structure of $Au_{32}Pt_6$ nanocluster at T = 1400 K. 117

Figure A 32 Atomic distance comparison graphs obtained from USR and structure of $Au_{32}Pt_6$ nanocluster at T = 1500 K. 118

Figure A 33 Atomic distance comparison graphs obtained from USR and structure of $Au_{32}Pt_6$ nanocluster at T = 1600 K. 119

Figure A 34 Atomic distance comparison graphs obtained from USR and structure of $Au_{32}Pt_6$ nanocluster at T = 1700 K. 120

Figure A 35 Atomic distance comparison graphs obtained from USR and structure of $Au_{32}Pt_6$ nanocluster at T = 1800 K. 121

Figure A 36 Atomic distance comparison graphs obtained from USR and structure of $Au_{32}Pt_6$ nanocluster at T = 1900 K. 122

Figure A 37 Atomic distance comparison graphs obtained from USR and structure of $Au_{32}Pt_6$ nanocluster at T = 2000 K. 123

LIST OF ABBREVIATIONS

BCGA	Birmingham Clusters Genetic Algorithm
BH	Basin Hopping
BTIMD	Brownian Type Isothermal Molecular Dynamics
CCM	Atom Closest to the Centre of Mass
CCS	Cubic Coupling Scheme
COM	Centre of Mass
FCM	Atom Farthest from the Centre of Mass
FTF	Atom Farthest to Atom Farthest from the Centre of Mass
GA	Genetic Algorithm
MBH	Multicanonical Basin Hopping
MD	Molecular Dynamics
PES	Potential Energy Surface
PTMBHGA	Parallel Tempering Multi-Canonical Basin Hopping plus Genetic Algorithm
RMS	Root-mean-square
USR	Ultrafast Shape Recognition
VMD	Visual Molecular Dynamics

LIST OF SYMBOLS

n	Cluster size, or number of atoms
T	Temperature
${}^{N}P_{A,B}$	Number of homotops
A_{ij}	Coefficient of repulsive pair term
ξ_{ij}	Effective hopping integral between i and j
p_{ij}	Dependence on the repulsive interatomic distance between i and j
q_{ij}	Dependence on the attractive interatomic distance between i and j
$r_{ij}^{(0)}$	Equilibrium first neighbour distance
f_i	Fitness value of candidates cluster i
V_{max}	Maximum energy cluster in the population
V_{min}	Minimum energy cluster in the population
$V(x)$	Potential energy
V_i	Potential energy of ith atom
V_h	Highest potential energy
V_l	Lowest potential energy
E_{old} ,E_{new}	Local minimum energy

$\tilde{E}(X)$	Transformed energy topology
β	Confidence level
w_{mu}	The non-Boltzmann multicanonical weight factor
$\beta^{mu}(\tilde{E})$	Effective inverse temperature
$\alpha^{mu}(\tilde{E})$	Multicanonical parameter
$x_{i(a)}$, $x_{i(b)}$	x-component position coordinate
$p_{i(a)x}$,$p_{i(b)x}$	x-component momentum
E_n	Potential energy defined from the Gupta many-body potential
$\mu_{a,x}$,$\nu_{a,x}$,$\eta_{a,x}$	Spherical Gaussian as a function of vector position $\boldsymbol{r_i}$ of atom i
$p_{0,a}$	Average thermal momentum
d_0	Dimensionless constant
L_0	Constant with dimension of length
$e_{0,a}$	Energy constant
ω_D	Debye frequency
Δt	Time step
ζ	Shape similarity index
m	Total number of statistical moment descriptors

$\Delta_2 E$	Second energy difference
C_v	Specific heat
δ	Lindemnn index
r_{ij}	Relative bond length
$P(\zeta)$	Probability distribution function of shape similarity index

SIFAT-SIFAT TERMA DAN STRUKTUR KEADAAN ASAS NANOKLUSTER TULEN DAN PANCALOGAM MELALUI SIMULASI DINAMIK MOLEKUL

ABSTRAK

Dalam bidang fizik komputasi, sifat terma nanokluster adalah antara topik yang biasa dikaji melalui simulasi dinamik molekul. Walau bagaimanapun, kaedah pasca-proses data dan penentuan julat pra-pencairan serta peleburan nanokluster pada komposisi tertentu adalah berbeza bagi setiap penyelidikan. Dalam tesis ini, kajian mengenai sifat terma bermula dengan memperoleh struktur keadaan dasar nanokluster emas-platinum 38-atom $\mathrm{Au}_n\mathrm{Pt}_{38-n}$ bagi pelbagai komposisi (di mana $0 \leq n \leq 38$) dengan mengguna algoritma *Parallel Tempering Multicanonical Basin Hopping plus Genetic Algorithm* (PTMBHGA). Nanokluster dwilogam $\mathrm{Au}_{32}\mathrm{Pt}_6$ dengan simetri D_{6h} telah dipilih untuk perincian lanjutan sifat-sifat termanya memandangkan ia merupakan nanokluster dwilogam yang paling stabil dalam tesis ini. Kod dinamik molekul yang dikenali sebagai *Brownian type isothermal molecular dynamics* (BTIMD). Haba tentu, C_v dan indeks Lindemann, δ yang merupakan penghurai-penghurai yang lazim dalam memantau kelakuan peleburan nanokluster telah dikira untuk $\mathrm{Au}_{32}\mathrm{Pt}_6$. Lengkungan C_v yang diperolehi menunjukkan bahawa peleburan nanokluster ini berlaku di antara T =1000 K dan 1050 K. Kewujudan fasa pra-peleburan dalam kalangan nanokluster telah dibuktikan melalui lengkungan C_v dan δ yang menunjukkan peningkatan secara mendadak pada $T = 700$ K sehingga $T = 800$ K. Kod *Ultrafast Shape Recognition* (USR) telah diperkenalkan untuk memperinci fenomena pra-peleburan. Data yang terkumpul diplotkan dalam bentuk jarak atom dan fungsi taburan kebarangkalian bagi indeks keserupaan bentuk.

Kedua-dua hasil kajian tersebut telah megesahkan secara berdikari bahawa pra-peleburan berlaku di antara $T = 760$ K dan 770 K. Berbagai-bagai pendekatan komputasi yang dicuba di dalam tesis ini memeperlihatkan keputusan-keputusan yang tertumpu untuk julat pra-peleburan dan peleburan nanokluster-nanokluster yang dikaji. Di antara kaedah-kaedah tersebut, pendekatan USR yang memeberi gambaran yang terperinci terhadap kelakuan peleburan nanokluster. Kaedah ini telah membuktikan ia sendiri sebagai penghurai yang lebih tepat berbanding dengan haba tentu, C_v dan indeks Lindemann, δ.

THERMAL PROPERTIES AND GROUND-STATE STRUCTURES OF PURE AND ALLOY NANOCLUSTERS VIA MOLECULAR DYNAMICS SIMULATION

ABSTRACT

The study of thermal properties of nanoclusters via molecular dynamics simulation is a common research topic in computational physics. However, the methods of post-processing and determining the pre-melting and melting range of nanoclusters at specific composition differ in every research. In this thesis, the study of thermal properties was started by obtaining the ground-state structure of 38-atoms gold-platinum nanoclusters $Au_nPt_{38-n}$of various composition (where $n = 0,1, \dots ,38$) using Parallel Tempering Multicanonical Basin Hopping plus Genetic Algorithm (PTMBHGA). Bimetallic nanocluster $Au_{32}Pt_6$ with D_{6h} symmetry has been selected for further investigation in the thermal properties, as it is the most stable bimetallic nanocluster studied in this thesis. To study the melting mechanism of the clusters, a molecular dynamics code known as Brownian type isothermal molecular dynamics (BTIMD) was used. Specific heat, C_v and Lindemann index, δ, which are the common descriptors used to monitor the melting behaviour of clusters were calculated for $Au_{32}Pt_6$. The C_v curve revealed that the melting of this nanocluster commenced between T =1000 K and 1050 K. Both C_v and δ curves showed drastic increase at T = 700 K to T = 800 K, indicating the presence of pre-melting phase in nanoclusters. To scrutinize the pre-melting phenomena, ultrafast shape recognition (USR) code has been introduced. The data was plotted into atomic-distance plots and probability distribution function of shape similarity index. Both these two results independently proved that the pre-melting stage occurred between T = 760 K and 770 K. Various independent computational methods attempted in this thesis shown

convergent results in the pre-melting and melting range of the studied nanoclusters. Amongst these methods, the USR approach provided the most detailed insight to the melting behaviour of the nanaoclusters. It has proven itself to be a more precise as indicator compared to specific heat, C_v and Lindemann index, δ.

CHAPTER 1

INTRODUCTION

The size of an atom ranges from 1×10^{-10} m to 5×10^{-10} m, which is about 0.1 to 0.5 nanometre. When few or more atoms group together, they form a minute atomic structure which is about the size of a nanometre. Due to the advancement of nanotechnology, these atomic structures have been studied extensively. In this thesis, thermal properties of atomic lattices in the nanometric scale are studied. These atomic lattices will then be regarded as "nanoclusters".

1.1 Nanoclusters

Nanocluster is a group of particles (atoms or molecules) with its size in the order of nanometre (10^{-9} m) formed by any countable number of atoms (2 to 10n, where n can be up to 6 or 7) (Johnston 2002, pp. 25) that are combined together (Logsdail 2011, pp. 2). Nanoclusters can be formed from identical atoms (homo-atomic) or two or more types of atoms (hetero-atomic). An example of homo-atomic nanoclusters is platinum nanocluster, Pt (Saxena *et al.* 2011). A good example of hetero-atomic nanocluster is silicon carbon nanocluster,SiC (Pradhan *et al.* 2004). Each type of clusters has their own uniqueness that make them a worthwhile topic to study.

Nanoclusters can also be classified according to the types of element from which the clusters are comprised of. The classification includes metallic nanoclusters (metallic elements), semiconductor nanoclusters (carbon, silicon and germanium), ionic nanoclusters (elements that involve ionic or electrostatic bonding), rare gas nanoclusters (elements from helium to radon in group 18), molecular nanoclusters (formed from supersonic expansion of molecular vapour) and nanocluster molecules (inorganic and organometallic nanoclusters). The clusters to be studied in this thesis are specific types of metallic nanoclusters. Metallic clusters are formed by elements with metallic bonding, which includes the simple s-block alkali and alkaline earth metals (from group 1 and 2 in periodic table) and transition metals with valance d orbitals (Johnston 2002, pp. 26).

Due to high surface area to volume ratio in nanoclusters, their physical properties generally display a size-dependence behaviour. The surface energy contribution is playing an important role in the study in the study of nanoclusters (Baletto *et al.* 2005). As a result, nanoclusters of different sizes will exhibit different properties despite being formed by the same elements.

1.2 Importance of Nanoclusters

The increasing interest in nanoclusters throughout the past decades is due to the possibilities of them having distinct physical and chemical properties compared to bulk state (Ferrando *et al.* 2008). The potential applications of nanocluster technology in physics, chemistry, biology, medicine and our daily life have accelerated the progress of research on nanoclusters. The application of nanocatalysis in industry, hydrogen storage and high sensitivity magnetic sensors have become the

factors that drive researchers to study further into nanoclusters (Carabineiro *et al.* 2007) (Van Dijk 2011, pp. 3). The research community has been attracted by its ability to control the chemical reactivity and physical properties of nanoclusters to form new materials that can be tailored according to the requirements in industrial applications.

To understand the properties of nanoclusters, researchers have searched for the most stable structures with the lowest potential energy (Baletto *et al.* 2005). After finding the geometrical and electronic structure of nanoclusters, the results will be branched out to the studies of catalytic, magnetic, optical and thermal properties. Due to the limitation in current technology, the bare cluster without encapsulation is not stable and most of the time it has to be concealed with ligands. Since the properties of the nanoclusters are not easily measured in experiments, theoretical studies and computational methods have become important tools in development and application of nanocluster (Johnston 2002, pp. 29).

Most of the single element nanoclusters in periodic table had been studied widely. Motivated by the interest to fabricate intermetallic materials used in catalysis, engineering and electronics, bimetallic and trimetallic nanoclusters with the flexibility to control the structure and properties have drawn widespread interest among researchers (Ferrando *et al.* 2008). The range of properties for bimetallic and trimetallic nanoclusters can be widely enhance by tuning the size, atomic ordering and compositions. The structures obtained from bimetallic nanoclusters can differ from pure nanoclusters with the same number of atoms, hence some bimetallic nanoclusters with magic size and compositions will possess strong stability.

From theoretical point of view, the idea of "homotops" have been introduced to describe the isomers of bimetallic nanocluster A_xB_y with fixed number of atoms $(N = x + y)$ and composition $(x/y \text{ ratio})$ which have identical geometrical arrangement but with A and B types of atoms arranged differently (Jellinek *et al.* 1996). A geometrical isomer of *N*-atom A_xB_y nanocluster will generate ${}^{N}P_{A,B}$ homotops, where

$$ {}^{N}P_{A,B} = \frac{N!}{N_A!N_B!} = \frac{N!}{N_A!(N-N_A)!} \tag{1.1} $$

N is the total number of atoms, N_A and N_B are the number of atoms of type A and type B respectively. From Equation (1.1), ${}^{N}P_{A,B}$ rises rapidly with the increase of N. As a consequence, the global optimization process to study bimetallic nanoclusters becomes increasingly complicated (Ferrando *et al.* 2008).

1.3 Gold-Platinum Nanoclusters

Gold (Au) with a filled d-orbital and atomic number 79 is a material which has been studied intensively due to its unique capability to hold as planar structure from 3 to 14 atoms in gold nanoclusters (Xiao *et al.* 2004a). Moreover, gold nanoclusters are relatively stable in acidic and alkaline solution (Tang *et al.* 2009). The stability of gold makes it unreactive in bulk form. However, it can become reactive in the form of a nanocluster. With the ability to resist bacterial infection, gold nanoclusters are widely used in medical field, including the microsurgery of ears and other surgery that require implants with the risk of infection (Giasuddin *et al.* 2012). Besides, gold nanoclusters serve as catalyst in the electrocatalytic oxidation of carbon monoxide (CO) in industry (Maye *et al.* 2000).

Meanwhile, platinum (Pt) is a transition element in periodic table with atomic number 78. It is an important catalyst in various industries, including part of catalyst in automotive catalytic converters to diminish toxic pollutants (Xiao *et al.* 2004b), oxygen reduction and polymer electrolyte membrane fuel cell (Tang *et al.* 2009). However, researcher are searching for a better alternative to reduce the involvement of platinum due to its limited supply, high cost and susceptibility to poisoning from oxidation products (Tang *et al.* 2009).

Gold-platinum nanoclusters are widely used in industrial as effective catalyst in oxygen reduction process (Wanjala *et al.* 2010) and fuel cell electrocatalysis (Maye *et al.* 2004). Furthermore, they have been investigated for methanol and CO electrooxidation (Piotrowski *et al.* 2012). The structures of gold-platinum nanoclusters have been investigated while the results show that they are immiscible in bulk form but experimentally proven that they can exist as nanoclusters (Mott *et al.* 2007).

1.4 Objective of Study

1. As clusters consist of gold and/or platinum are widely used in industries, it becomes an essential piece of information as what are the temperatures at which gold nanoclusters undergo structural changes. In order to know how gold-platinum nanoclusters are affected by temperature variation, we shall study their possible structures at high temperatures, as they are altered, as well as the melting behaviour of these nanoclusters.

2. In order to study the thermal properties of gold platinum nanoclusters of choice, their stable structures, or lowest-energy states, have to be identified. Several compositions of bimetallic gold platinum nanoclusters have been studied in the literature, including those with 40 (Leppert *et al.* 2011) and 55 atoms (Bochicchio *et al.* 2013).

3. Conventional methodologies to study thermal instabilities of nanoclusters, such as Lindemann index and specific heat capacity curve, turn out to be not sufficiently sensitive to capture the melting behavior during the pre-melting phases. Quantifying the melting behaviour of nanoclusters during pre-melting phases is essential to understand the changes that occur within the nanocluster as temperature varies. In the thesis, a novel approach is proposed to quantify and capture these details.

CHAPTER 2

THEORETICAL BACKGROUND AND METHODOLOGIES

The main issue this thesis wishes to address is about the structural and thermal behaviour of gold-platinum clusters. To this end, a specific global optimization search algorithm named Parallel Tempering Multicanonical Basin Hopping plus Genetic Algorithm (PTMBHGA), is used to generate the ground state structure of a given atom composition starting from a random configuration. Once the clusters with minimal energies have been obtained as an end output from a completed PTMBHGA run, they will be subjected to molecular dynamics (MD) thermal evolution. The specific MD algorithm used is known as Brownian type isothermal molecular dynamics simulation. The energy calculator used to calculate the potential energy of the atomic configurations generated during the process of global minimum search in the PTMBHGA algorithm, which is also the same as that used in the MD simulation, is the Gupta potential. The MD evolution using a purpose-specific numerical algorithm known as ultrafast shape recognition. It is meant to abstract in a frame-by-frame manner information of the atomic configurations so that the detailed mechanism of the melting procedures occurring during the thermal evolution of the system can be statistically quantified. The overall flow of the calculation procedure is shown in the flow chart in Figure 2.1.

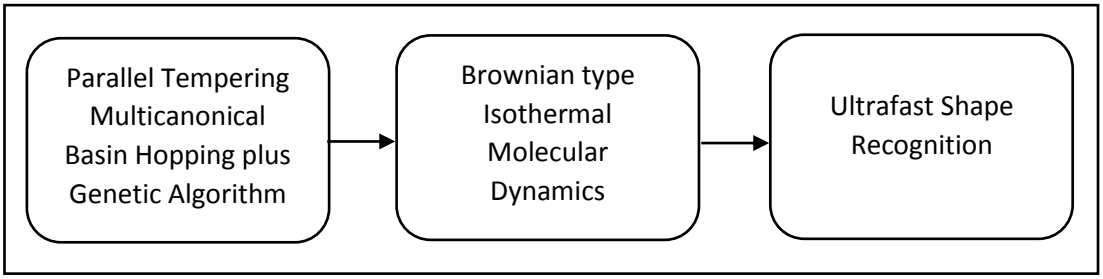

Figure 2.1: Flow chart of calculation procedure.

The main components of the calculation procedure in the flow chart are explained in the following subsections.

2.1 Parallel Tempering Multicanonical Basin Hopping Plus Genetic Algorithm (PTMBHGA)

The first step in the theoretical study of a nanocluster is to identify its ground-state structure which is, by definition, its lowest energy state. Identification of ground-state structure is the first most important task before one can advance into calculating the physical properties of a cluster. In principle, all measurable observables of a nanoclusters can be derived theoretically if its ground state is known. Semi-empirical methods such genetic algorithm and basin hopping, which work as global energy optimizers, are commonly used in the search for ground-state structure. As an example, Birmingham Clusters Genetic Algorithm (BCGA) is a genetic algorithm developed by R.L. Johnston as global minimum search algorithm (Johnston 2003). BCGA have been applied in various studies from ionic clusters, metal clusters to bimetallic clusters, such as CuAu nanoclusters (Darby *et al.* 2002) and PdPt nanoclusters (Massen *et al.* 2002). Another global minimal search algorithm to mention here is Parallel Tempering Multicanonical Basin Hopping plus

Genetic Algorithm (PTMBHGA) (Hsu *et al.* 2006). The latter will be used in this thesis as the global minimum searching tool.

Parallel Tempering Multicanonical Basin Hopping plus Genetic Algorithm (PTMBHGA) is a software package developed by the Complex Liquid Lab in the National Central University, Taiwan (Hsu *et al.* 2006). PTMBHGA was designed to compute the lowest energy geometries (ground-state structures) of bimetallic nanoclusters. Their searching technique combines both basin hopping and genetic algorithm, and is claimed to improve the potential energy surface (PES) search and resolve the issue of calculations being trapped in local minima.

2.1.1 Gupta Many Body Potential

In order to calculate the interactions between many-body atoms, n-body Gupta potential is employed. The empirical potential is written as:

$$E_n = \sum_{i=1}^{n} \left\{ \begin{array}{l} \sum_{j=1(j\neq i)}^{n} A_{ij} exp\left(-p_{ij}\left(\frac{r_{ij}}{r_{ij}^{(0)}}-1\right)\right) - \\ \left[\sum_{j=1(j\neq i)}^{n} \xi_{ij}^{2} exp\left(-2q_{ij}\left(\frac{r_{ij}}{r_{ij}^{(0)}}-1\right)\right)\right]^{1/2} \end{array} \right\} \qquad (2.1)$$

A_{ij}, ξ_{ij}, p_{ij}, q_{ij} and $r_{ij}^{(0)}$ are parameters fitted to bulk quantified data by Cleri and Rosato for cohesive energy, lattice constant and elastic constant for face centred cubic crystal structure at 0 K (Cleri *et al.* 1993). A_{ij} is coefficient of repulsive pair term, ξ_{ij} is the effective hopping integral between i and j, p_{ij} and q_{ij} describe the dependence on the repulsive and attractive interatomic distance between i and j, $r_{ij}^{(0)}$ is the equilibrium first neighbour distance.

The parameters used in this work, including those for gold atoms (Au-Au), platinum atoms (Pt-Pt) and gold platinum atoms (Au-Pt), are listed in Table 2.1.

Table 2.1: Gupta parameters for gold, platinum and gold platinum atoms.

	p	q	$A(eV)$	$\xi(eV)$	r_0(Å)
Au-Au	12.229	4.036	0.2061	1.79	2.884
Pt-Pt	10.621	4.004	0.2795	2.695	2.7747
Au-Pt	10.42	4.02	0.25	2.2	2.8294

2.1.2 Genetic Algorithm

Genetic algorithm (GA) is a global minimum search algorithm developed from the inspiration of evolution process. It was first used in the 1970s by John Holland from University of Michigan (Borbón 2011). He proposed four basic elements for a generic GA algorithm, namely, encoding scheme, fitness function, selection methods and lastly the genetic operator (Yen 2015).

The particular flavour of GA as implemented in the PTMBHGA code follows the scheme as described below. The process starts from encoding a three dimensional coordinates of initial population (x, y, z) into one dimensional coordinates $(X_1, X_2,\ldots,X_i)$, with $i = 3 \times$ the number of atoms of the initial population. It is then followed by the calculation of the potential energy using Gupta potential and the computation of local minima using conjugate gradient minimization (L-BFGS) method. The local minima obtained will then undergo the fitness evaluation (for certain populations) using the equation:

$$F_i = (V_{max} - V_i)/(V_{max} - V_{min}) \tag{2.2}$$

$$f_i = \frac{F_i}{\sum_{j=1}^{20} F_j} \tag{2.3}$$

where V_{max} and V_{min} are the maximum and minimum energy cluster in the population and f_i is the normalized fitness. The statistics obtained are used in the formation of "children" (next generation) of the GA calculations. 75% of the "parents" individuals will be retained for the creation of next generation individuals. The "parents" individuals with higher fitness will undergo five genetic operators which include inversion, arithmetic mean, geometric mean, n-point crossover and 2-point crossover to sort out the "children" individuals (Lai *et al.* 2002).

The GA process is repeated until it fulfils either one of the criterion, which is, the potential energies obtained remains unchanged for a few steps, or, the simulations end with the steps fixed at the beginning of the GA process configurations.

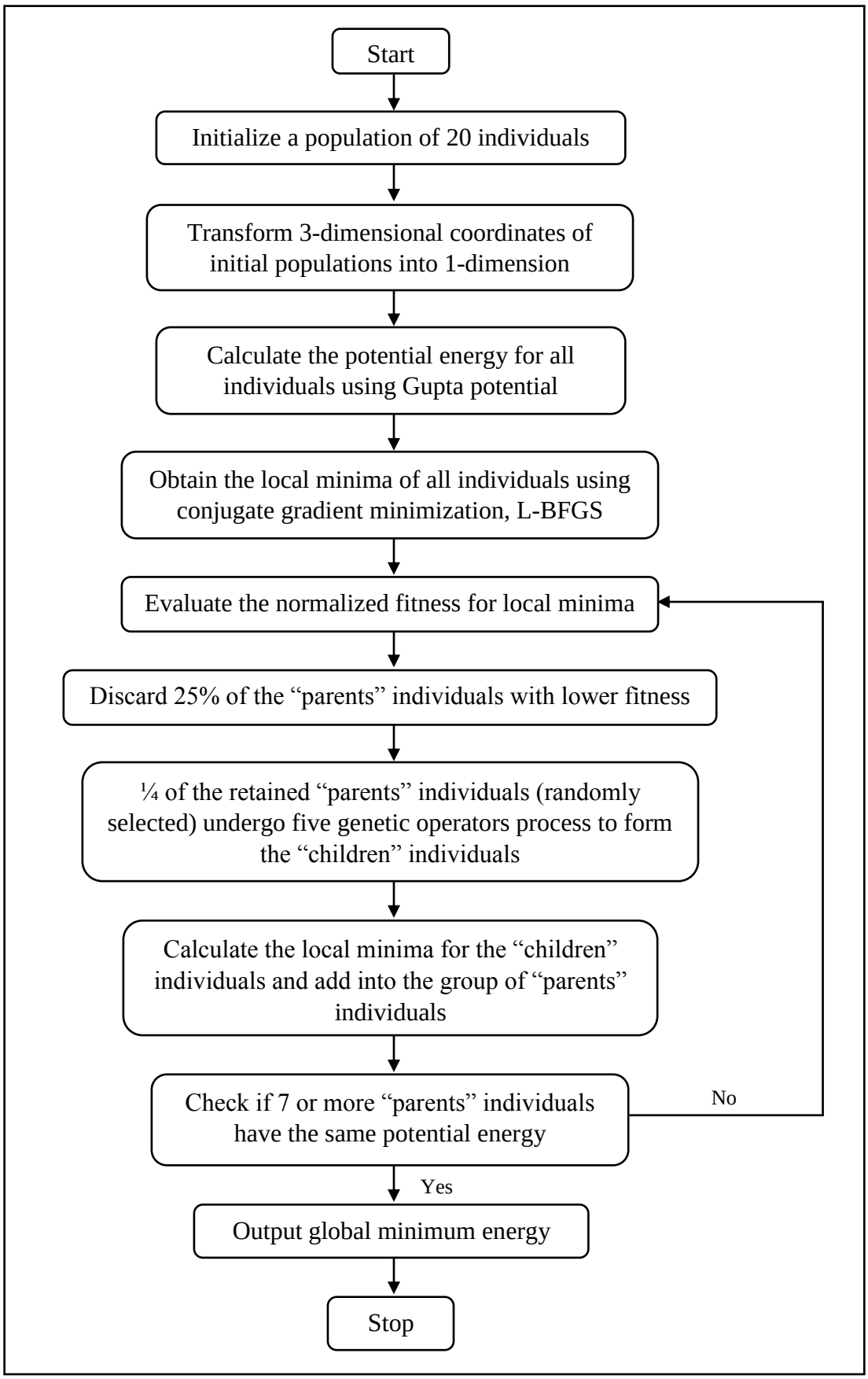

Figure 2.2: Flow chart of genetic algorithm in PTMBHGA.

2.1.3 Basin Hopping

Basin hopping is a potential energy surface analysis which searches for a global minimum across the potential energy landscape of a system formed by a lot of local minima (Zhan *et al.* 2004). This algorithm was proposed in 1997 by Wales and Doye to locate the global minimum structure for Lennard-Jones Clusters up to 110 atoms (Wales *et al.* 1997).

The end results of the potential energy surface analysis can be represented by the following equation:

$$\tilde{V}(X) = \min\{V(x)\} \tag{2.4}$$

where min denote the local-energy minimization and $V(x)$ represents the potential energy (Lai *et al.* 2002).

In the basin hoping algorithm, an initial random arrangement of the nanocluster is calculated numerically to obtain the local minimum energy of the nanocluster. The simulation starts with the calculation of the local minimum energy for the initial random coordinate generated. The local minimum energy, E_{old} obtained is then fit into equation:

$$E = \frac{1}{2}\sum_{i=1}^{n} V(i) \tag{2.5}$$

where V_i indicates the potential of ith atom caused by the interaction with all atoms in the nanocluster. The potential V_i , where $i = 1,2, \dots, n$ are inspected. The V_h(highest potential) and V_l (lowest potential) are sorted out. If $V_h > \upsilon V_l$ where υ is a constant initially set at 0.4, V_h is considered as the potential for atoms farthest away from the centre of mass and the potential for all the other atoms $(n - 1)$ are displaced

by δ, which is also a constant initially set as 0.36. Whereas if $V_h < \upsilon V_l$, all the atoms are displaced by δ.

After getting a new sets of potential, the local minimum energy E_{new} is calculated again with Equation (2.5). If the E_{new} calculated is smaller than E_{old}, it will directly replace E_{old} to be the local minimum energy used for the analysis part. The results are then tested if it falls within a certain confidence level, β, where $0 < \beta < 1$. The suitability of parameters δ and υ are tested until an optimum value of δ and υ are obtained. The process is repeated until it reached the pre-set maximum steps.

However, there are times where the simulation is unable to satisfy even the lowest confidence level due to the huge energy difference. To overcome this issue, genetic algorithm is introduced to the system in order to rearrange the system configuration.

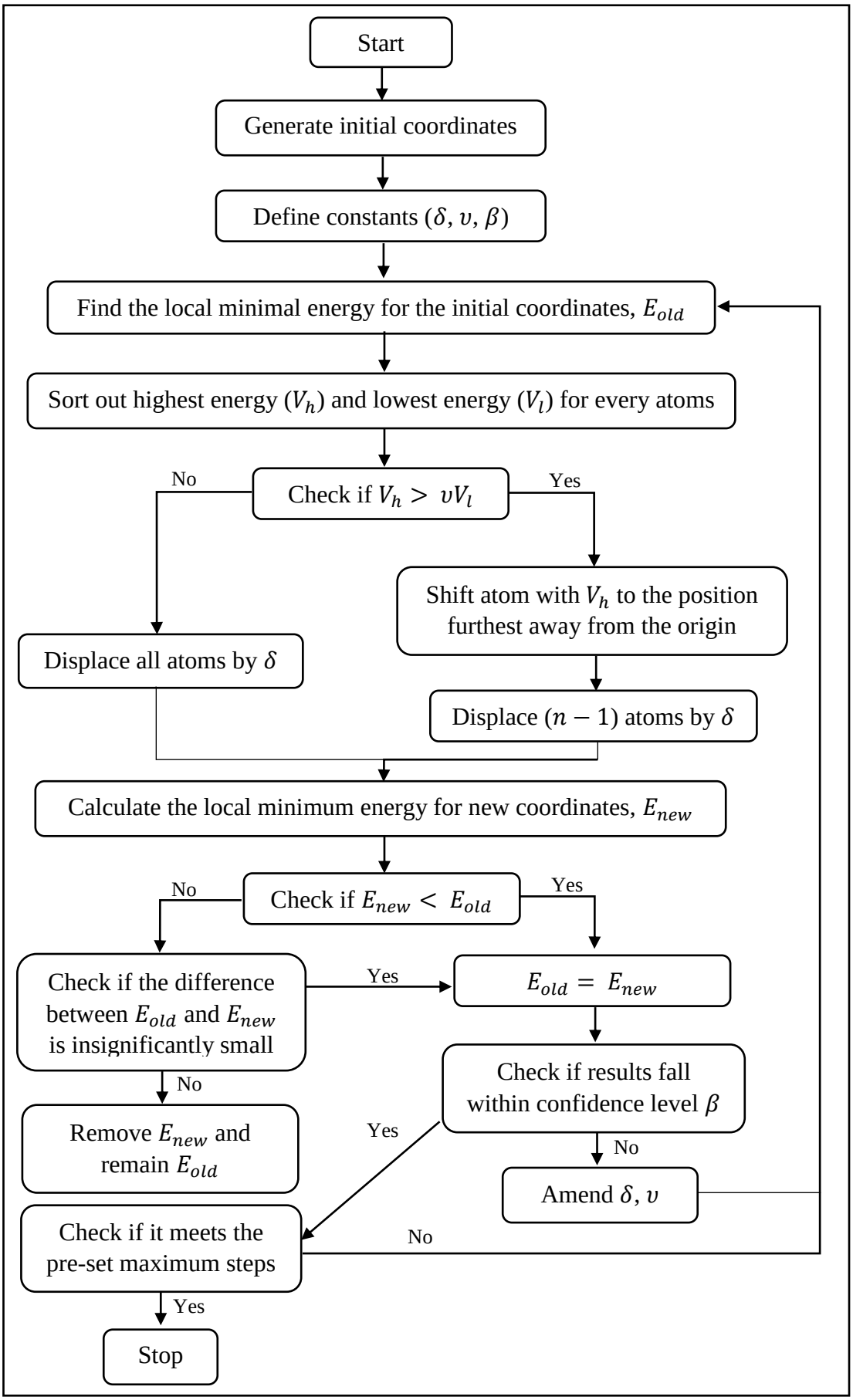

Figure 2.3: Flow chart of basin hopping in PTMBHGA.

2.1.4 Multicanonical Basin Hopping

For system involving large number of atoms, the chances of the basin hopping search to fall into a deep potential well in PES is high. Multicanonical basin hopping is introduced to overcome this issue. It is modified from the Boltzmannian Monte Carlo scheme. In terms of multidimensional staircase topography $\tilde{E}(X)$, the non-Boltzmann multicanonical weight factor can be written as:

$$w_{mu}(\tilde{E}) = e^{-\beta^{mu}(\tilde{E})\tilde{E}-\alpha^{mu}(\tilde{E})} \tag{2.6}$$

where $\beta^{mu}(\tilde{E})$ is an effective inverse temperature while $\alpha^{mu}(\tilde{E})$ is a multicanonical parameter (Hsu *et al.* 2006).

By applying the weigh factor into basin hopping simulation will help to flatten out the PES and raise the probability for the global minimum search to obtain structure with lower potential energy. The application of multicanonical basin hopping enable the lowest potential energy search to cover wider area in potential energy surface and thus increase the credibility of local potential minimum search.

2.1.5 PTMBHGA Working Parameters

In the PTMBHGA code developed by Hsu (Lai *et al.* 2002), the empirical Gupta many-body potential is used as the energy calculator. The calculation process involves 3 cycles of basin hopping and multicanonical basin hopping:

First cycle: BH for 100 steps and MBH for 10 steps

Second cycle: BH for 100 steps and MBH for 20 steps

Third cycle: BH for 100 steps and MBH for 30 steps

For the genetic algorithm simulations, PTMBHGA only preserve 75% of the parents' individuals and replace the remaining 25% with children individuals. The genetic operators used have been weighed as below:

Inversion: 5

Arithmetic mean: 1

Geometric mean: 1

N-point crossover: 5

2-point crossover: 5

The process is repeated with the formation of 20 parents' individuals (5 newly regenerated) to calculate the lowest potential energy. The simulations ended after 500 steps of GA, which is deemed sufficient for the simulation to obtain the global minimum energy.

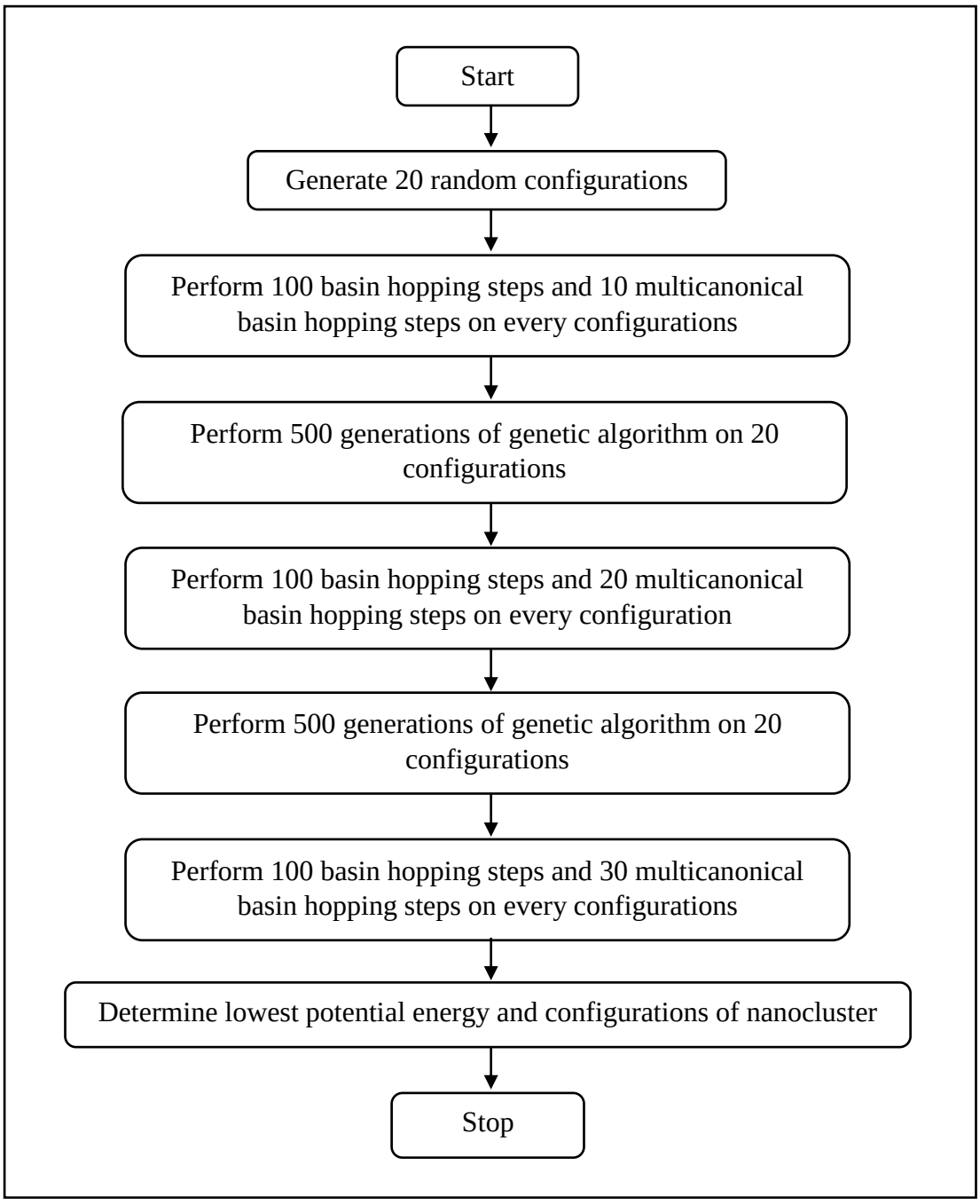

Figure 2.4: Flow chart of PTMBHGA.

2.2 Thermal Properties of Nanoclusters

Thermal properties of nanoclusters have been studied and observed since early of 20th century when Pawlaw explained the reduction in melting temperature of finite system. Thermal properties of a cluster can be studied through melting

process that involves the change in physical state of a matter as temperature varies. Exotic thermal properties found in certain clusters can find applications in e.g., biomedical field where the drugs can be encapsulated into substance made of small particles that melts just above human body temperature (Westesen 2000). Experimental studies on the melting of nanoclusters have been carried out at the end of 20th century by Schmidt *et al.* using sodium nanocluster (Kusche *et al.* 1999). In their studies, the nanocluster was heated and the results were compared with sodium in bulk form. The results proved that the melting temperature for nanocluster is lower than in bulk form (Schmidt *et al.* 1997). Besides, it was proven that the melting transitions of nanocluster does not happen at a finite temperature but spreading out to a finite temperature range. Meanwhile, in the theoretical front, molecular dynamics studies have suggested that melting in nanoclusters could display some unusual behaviour, e.g., emergence of pre-peaks in the melting curves and an extended temperature range throughout which melting is happening.

2.2.1 Brownian Type Isothermal Molecular Dynamics Simulations

In this section, the theoretical basis of Brownian type isothermal MD, will be discussed. Implementation of this MD approach in the form of a software package has been developed by S. K. Lai's team in National Central University, Taiwan. The team developed the code in year 2007 - based on the ideas inspired by Nose, Hoover and Kusnezov (Bulgac *et al.* 1990). The Brownian Type Isothermal Molecular Dynamics code (abbreviated BTIMD) used in this thesis is provided by the NCU group with kind courtesy.

The basic idea of this MD simulation approach is built upon canonical ensemble at classical level, and is designed with the intention to study melting behaviour of clusters (Yen *et al.* 2007). As in most MD approach to model thermodynamically related simulations, such as melting phenomena, temperature of the system has to be stipulated in a controlled manner. To this end, heat bath is coupled to the system to heat it up to a desired temperature. The temperature-tuning control in the MD simulation will require additional degree of freedom. In the case of BTIMD, the additional degree of freedom come in the form of pseudofriction terms that couple the heat bath to the simulated system via a cubic coupling scheme (CCS) which provides superiority over other MD approaches. The application of CCS managed to overcome the downsides of Nose-Hoover method, which are the dependency on (1) the assumption that the motion is ergodic, (2) the reliance of initial conditions, (3) algorithm parameters and, (4) pseudofriction terms (Kusnezov *et al.* 1990). The phase space of the system can be explored at fast exploration rate and ergodicity can be ensured (reproduced the canonical ensemble averages) with the involvement of CCS. The modified CCS involved three pseudofriction terms, which are sufficient to produce ergodic condition for free particles in contact with a thermal bath. The technical details of the CCS is compactly summarised in the equation below:

$$\dot{x}_{i(a)} = \frac{p_{i(a)x}}{m_a} \tag{2.7}$$

$$\dot{p}_{i(a),x} = -\frac{\partial E_n}{\partial x_{i(a)}} - \frac{\alpha_a e_{0,a}}{nL_0}\mu_{a,x}^3 \frac{p_{i(a),x}}{p_{0,a}} - \frac{\beta_a e_{0,a}}{nL_0}\nu_{a,x}\left(\frac{p_{i(a),x}^2}{p_{0,a}^2} - d_0\right) - \frac{\varkappa_a e_{0,a}}{nL_0}\eta_{a,x}\frac{p_{i(a),x}^3}{p_{0,a}^3} \tag{2.8}$$

$$\dot{\mu}_{a,x} = \frac{\alpha_a T}{p_{0,a}L_0}\left(\frac{\sum_{i=1}^{n_a} p_{i(a),x}^2}{nm_a T} + \frac{\sum_{i=1}^{n_b} p_{i(b),x}^2}{nm_b T} - 1\right) \tag{2.9}$$

$$\dot{v}_{a,x} = \frac{\beta_a T}{p_{0,a} L_0}\left(\frac{\sum_{i=1}^{n_a} p_{i(a),x}^3}{n m_a T p_{0,a}} + \frac{\sum_{i=1}^{n_b} p_{i(b),x}^3}{n m_b T p_{0,b}} - d_0 \frac{\sum_{i=1}^{n_a} p_{i(a),x} p_{0,a}}{n m_a T} - d_0 \frac{\sum_{i=1}^{n_b} p_{i(b),x} p_{0,b}}{n m_b T} - \frac{2\sum_{i=1}^{n_a} p_{i(a),x}}{n p_{0,a}} - \frac{2\sum_{i=1}^{n_b} p_{i(b),x}}{n p_{0,b}}\right) \quad (2.10)$$

$$\dot{\eta}_{a,x} = \frac{x_a T}{p_{0,a} L_0}\left(\frac{\sum_{i=1}^{n_a} p_{i(a),x}^4}{n m_a T p_{0,a}^2} + \frac{\sum_{i=1}^{n_b} p_{i(b),x}^4}{n m_b T p_{0,b}^2} - \frac{3\sum_{i=1}^{n_a} p_{i(a),x}^2}{n p_{0,a}^2} - \frac{3\sum_{i=1}^{n_b} p_{i(b),x}^2}{n p_{0,b}^2}\right) \quad (2.11)$$

In the equations 2.7 to 2.11, $x_{i(a)}$ and $x_{i(b)}$ are the x-component position coordinate, $p_{i(a)x}$ and $p_{i(b)x}$ are the x-component momentum, E_n is the potential energy defined from the Gupta many-body potential, $\mu_{a,x}$, $\nu_{a,x}$, and $\eta_{a,x}$ are the x-component pseudofriction coefficient, m_a is the atomic mas, $p_{0,a} = \sqrt{2m_a T}$ is the average thermal momentum at temperature T, d_0 is the dimensionless constant, L_0 is a constant with dimension of length, $e_{0,a}$ is the energy constant with value estimated from $e_{0,a} \sim m_a L_0^2 \omega_D^2/(4\pi^2)$, while ω_D is the Debye frequency, $\alpha_a \sim \beta_a \sim \varkappa_a \sim [\frac{m_a L_0^2}{n T t_0^2}]^{1/2}$, in which $t_0 = 2\pi/w_D$.

2.2.2 Procedures of Molecular Dynamics Simulations

All the MD simulations in this thesis were conducted using the BTIMD code provided by the NCU group. Throughout all simulations, time step of Δt which is fixed between 1×10^{-15} to 5×10^{-15} s was used. For lower temperature ($T \leq 500$ K), the simulation runs were carried out for a total of 1×10^8 steps so that the effect of large fluctuations during the melting can be circumvented by sampling a large amount of data via a lengthy simulation. Meanwhile, for gold-platinum nanocluster at higher temperatures ($550\ \text{K} \leq T \leq 1050\ \text{K}$), 2×10^8 steps were performed to produce smoothened resulting graphs and improve the reliability of the

simulation results. At the end of 2×10^8 steps run for case of temperature, $T \geq$ 1100 K, an additional 2×10^7 steps were carried out. The total elapsed time t_{tot} for a complete simulation was always fixed at 1×10^{-7} s.

The MD simulations were run at an interval of 50 K throughout all temperatures. However, in pre-melting and melting regions, which generally lies in the range of $700 \text{ K} \leq T \leq 1050$ K, a more refined interval of 10 K is adopted.

2.3 Ultrafast Shape Recognition

Molecular shape recognition technique is widely applied in chemistry field to categorize molecular structures, especially proteins structure. It has been experimentally proven to be an important tool to discover new materials (Boström *et al.* 2006). There are currently 2 types of shape recognition algorithm, namely, superposition-based shape comparison and superposition free algorithm (Ebalunode *et al.* 2010). The superposition-based shape similarity comparison algorithm was introduced in 1991 (Meyer *et al.* 1991). The downside of this algorithm is the time-consuming optimization process. To overcome this weak point, superposition-free algorithm that is based on the interatomic distance has been invented. This technique was named as Ultrafast Shape Recognition (USR) in a paper published in 2007 by Ballester *et al.* The technique has successfully speeded up the process of fast virtual screening (Ballester *et al.* 2009). The idea of USR ideology was inspired S. K. Lai's team from National Central University, Taiwan to come up with a novel approach for analysing metallic clusters undergoing thermodynamic transition.

The analysing process of USR involved the shape similarity index and probability of shape similarity function. It compares the reference ground-state

configuration of the original nanocluster at 0 K against the configuration at each time step during the simulation. The shape similarity index ζ is the quantifier used to measure the difference between the structures of the nanoclusters $i = 0$. Referring to Ballester *et al.*, shape similarity index is defined as

$$\zeta_i = \left[1 + \sum_{j=1}^{m} \left| M_{i,j} - M_{0,j} \right| / m \right]^{-1} \tag{2.12}$$

where i refers to the ith structural arrangement of the system at a given instance in a MD simulations. m is the total number of statistical moment descriptors to be included in the definition of ζ. The reference structure has the value $\zeta_i = 1$ when $i = 0$. Therefore, the value of ζ_i is less than 1 for any ith structure arrangements that is different from the reference structure. $\{M_{0,1}, M_{0,2}, \dots, M_{0,m}\}$ refer to the moments of atomic distance distribution of the reference structure, while $\{M_{i,1}, M_{i,2}, \dots, M_{i,m}\}$ refer to that of the ith arrangement.

Given the collection of a cluster's statistical data generated in a MD simulation, 4 different statistical moments, which are defined based on the 3D spatial coordinates of the atoms, can be defined, namely,

(i) Mean value

(ii) Variance

(iii) Skewness

(iv) Kurtosis

These moments in turns can be calculated by referring to 4 different reference sites (origins), namely,

(i) Centre of mass (COM)

(ii) Atom closest to the centre of mass (CCM)

(iii) Atom farthest from the centre of mass (FCM)

(iv) Atom farthest to atom farthest from the centre of mass (FTF)

Hence, overall, 16 different statistical moment descriptors can be discerned (only 12 moments are formally identified in Ballester *et al.* 2007). In other words, $m = 16$ as appear in the summation in Equation (2.12).

The definitions of 4 reference sites are given below, along with illustrating examples to facilitate the explanation.

(i) Centre of mass (COM)

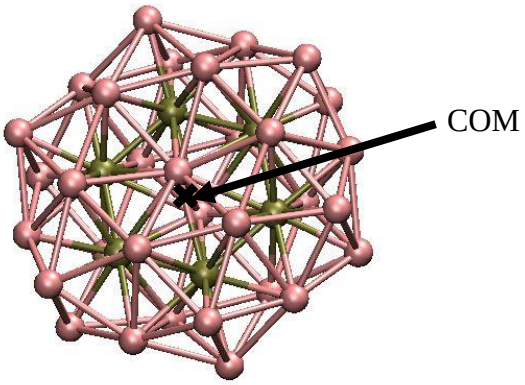

Figure 2.5: The location of COM in $Au_{32}Pt_6$ ground-state structure. (Olive green represents platinum atoms and pink represents gold atoms)

Centre of mass refers to the mean position of all the individual atoms in the nanocluster. Generally, COM of a given cluster may not coincide with any particular atom sitting inside the cluster. Rather, it may fall on a spatial point located in an